Figure 1: Temperature for January simulated in a radiative-convective model (Fels, 1988) (top). Corresponding observed zonal mean temperature from CIRA (Fleming et al., 1988) (bottom). The warm winter pole and cold summer pole in the mesosphere in the observations is a consequence of dynamical heating and cooling from breaking GWs.
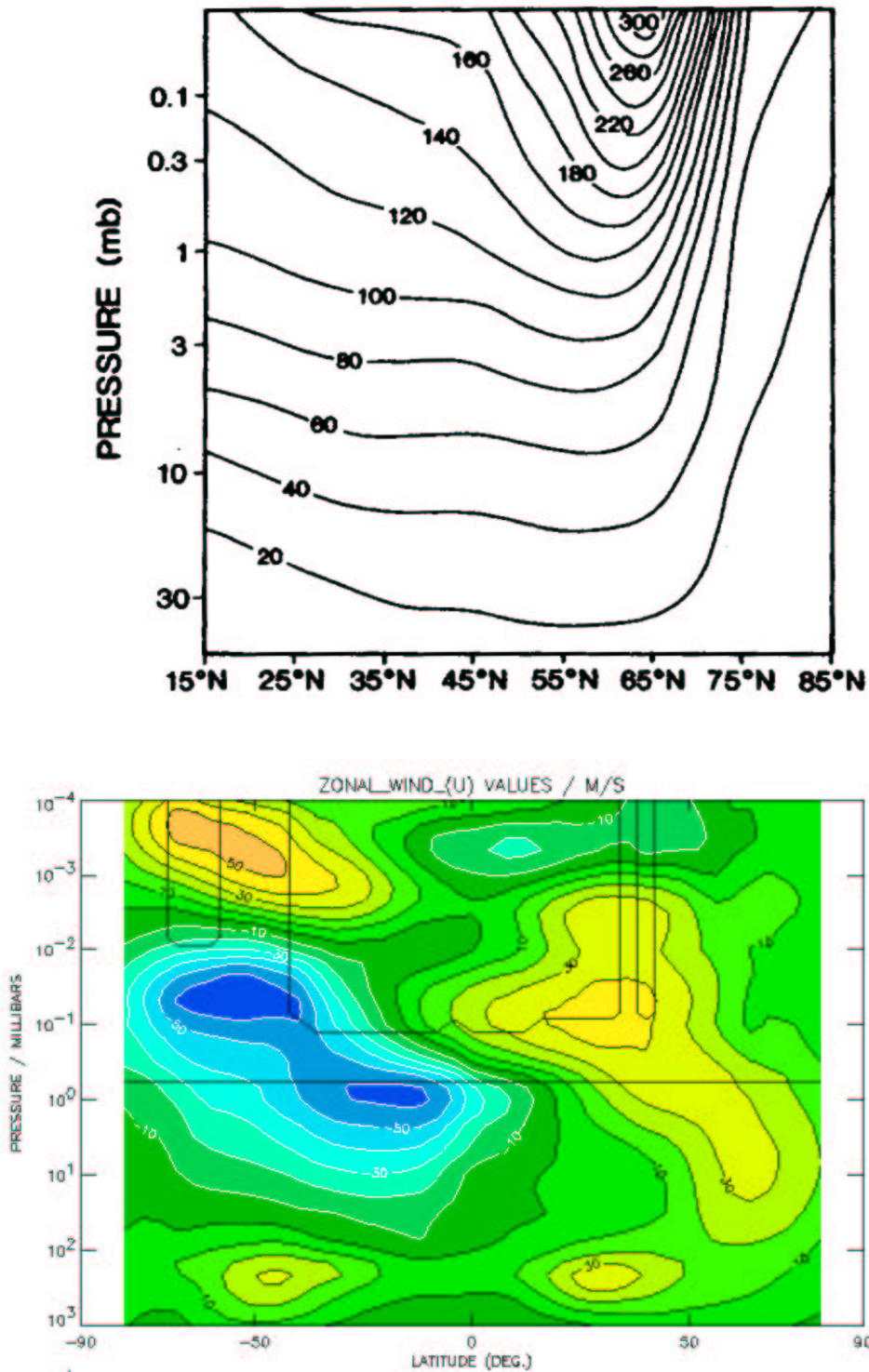
Figure 2: Zonal wind computed from the radiative-equilibrium temperature shown in Figure 1 using gradient-wind balance (top). Observed zonal mean zonal winds for January from the Upper Atmosphere Research Satellite Reference Atmosphere (bottom).
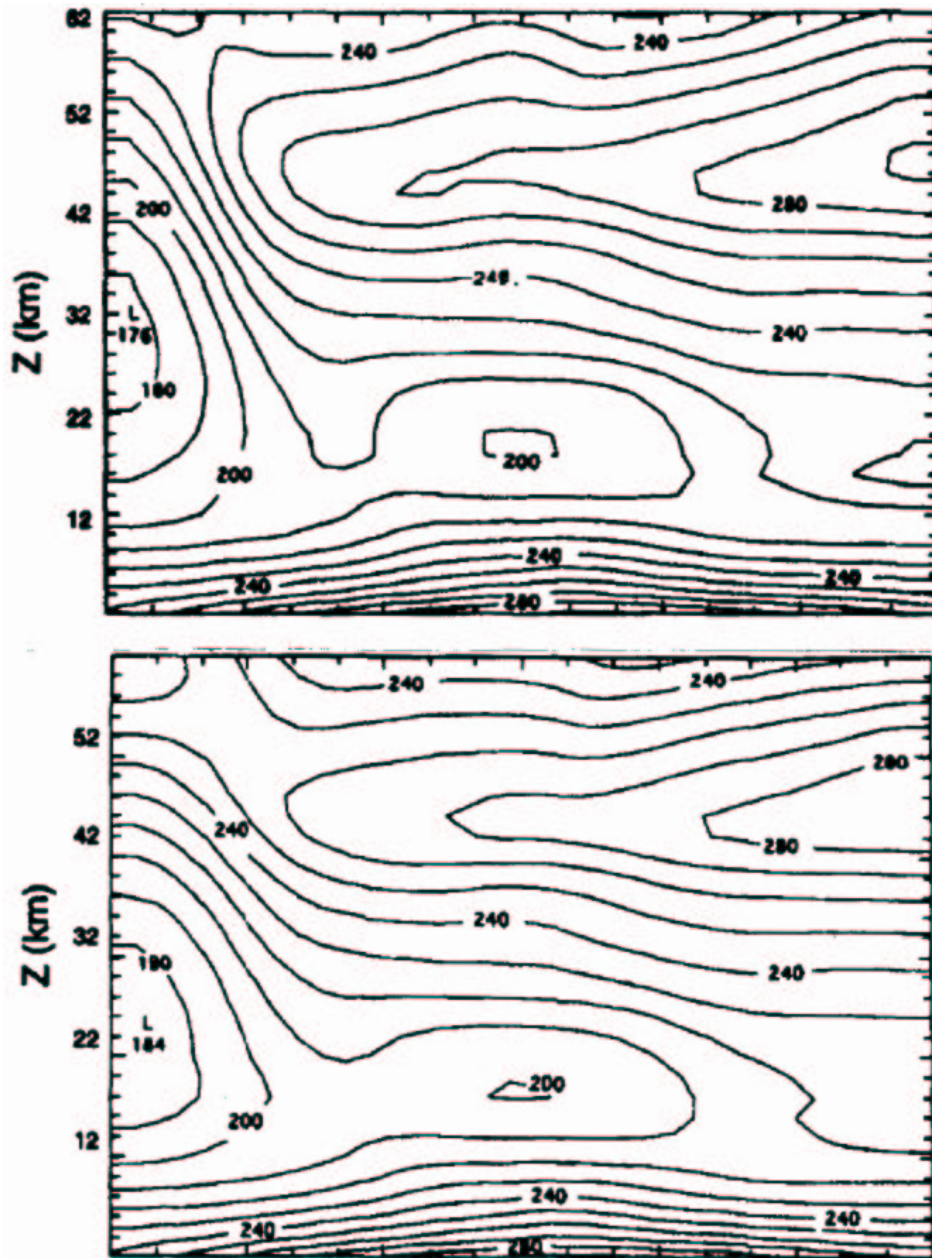
Figure 3: Zonal mean temperature for July computed using a two-dimensional model without GWD (top) and with GWD (bottom) (Garcia and Boville, 1994). The winter polar stratosphere, where radiative time scales are long, is considerably warmer in the simulation with GWD; this is a consequence of "downward control".
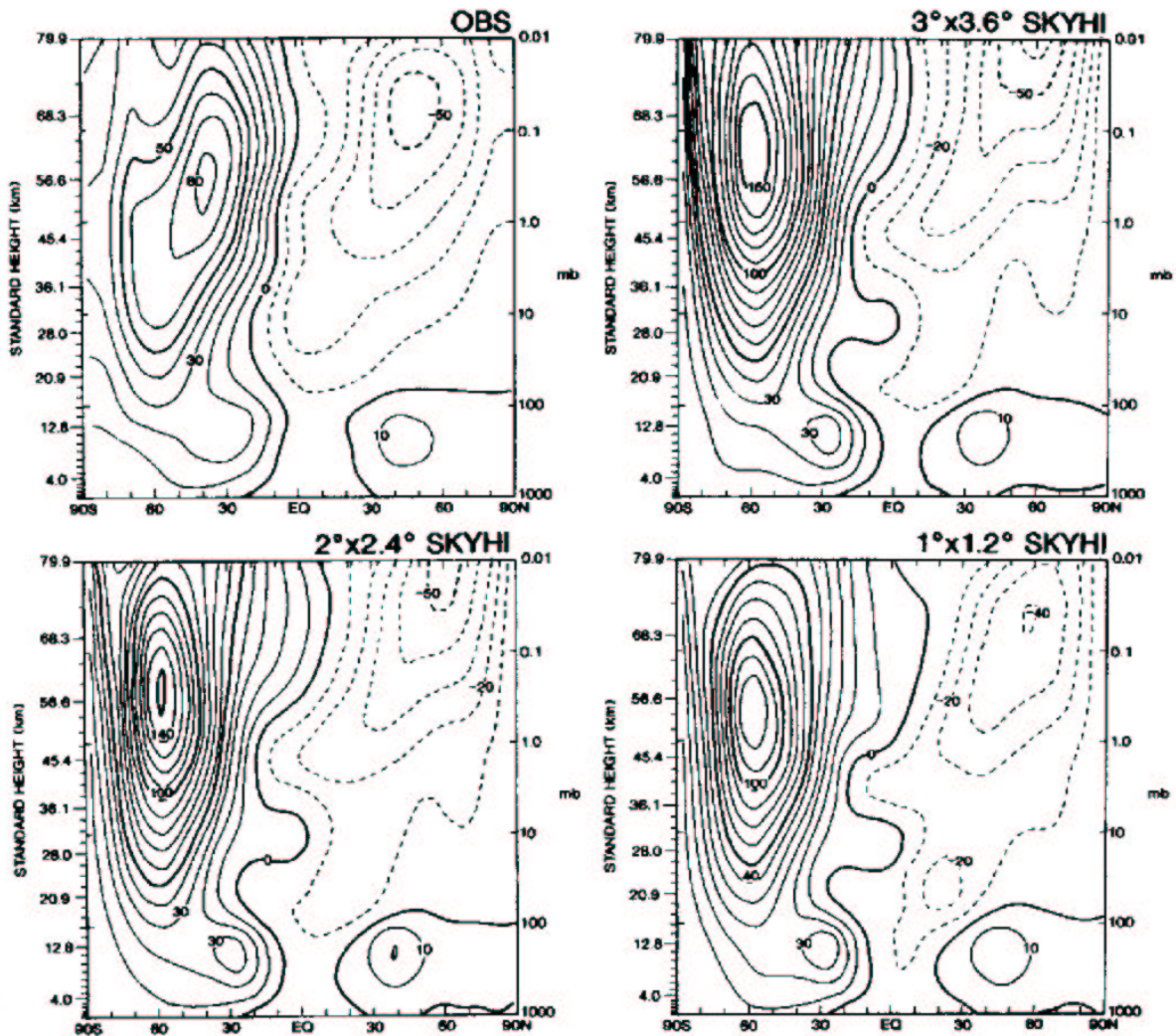
Figure 4: Zonal mean zonal winds for July computed using the SKYHI GCM for three different horizontal resolutions (Hamilton, 1996). The observed winds from CIRA are shown at top left. The weakening of the winter jet as the resolution is increased is attributed to the small-scale GWs.
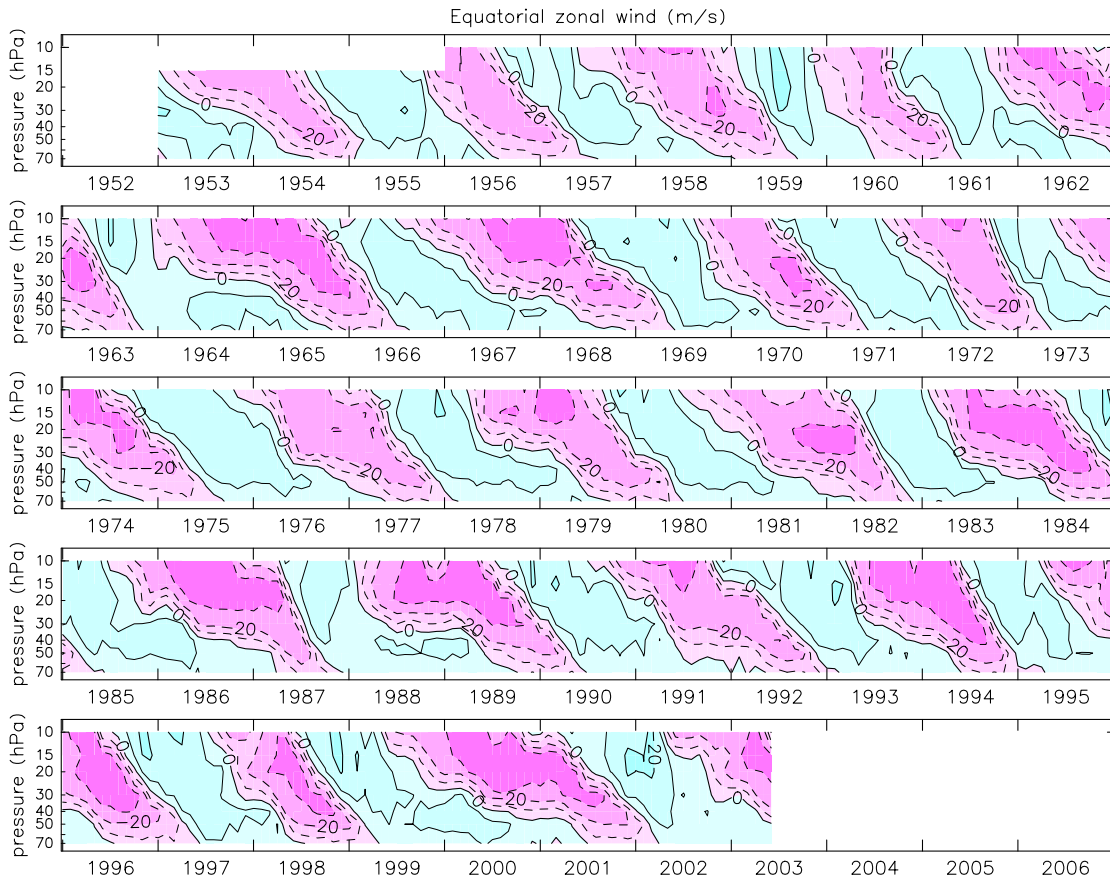
Equatorial zonal wind (m/s)

Figure 5: Observed equatorial monthly mean zonal winds derived from data from radiosonde stations at Canton Island, Gan-Maledive Islands and Singapore (Naujokat, 1986). Contour interval is 10 m/s; westerlies are blue.
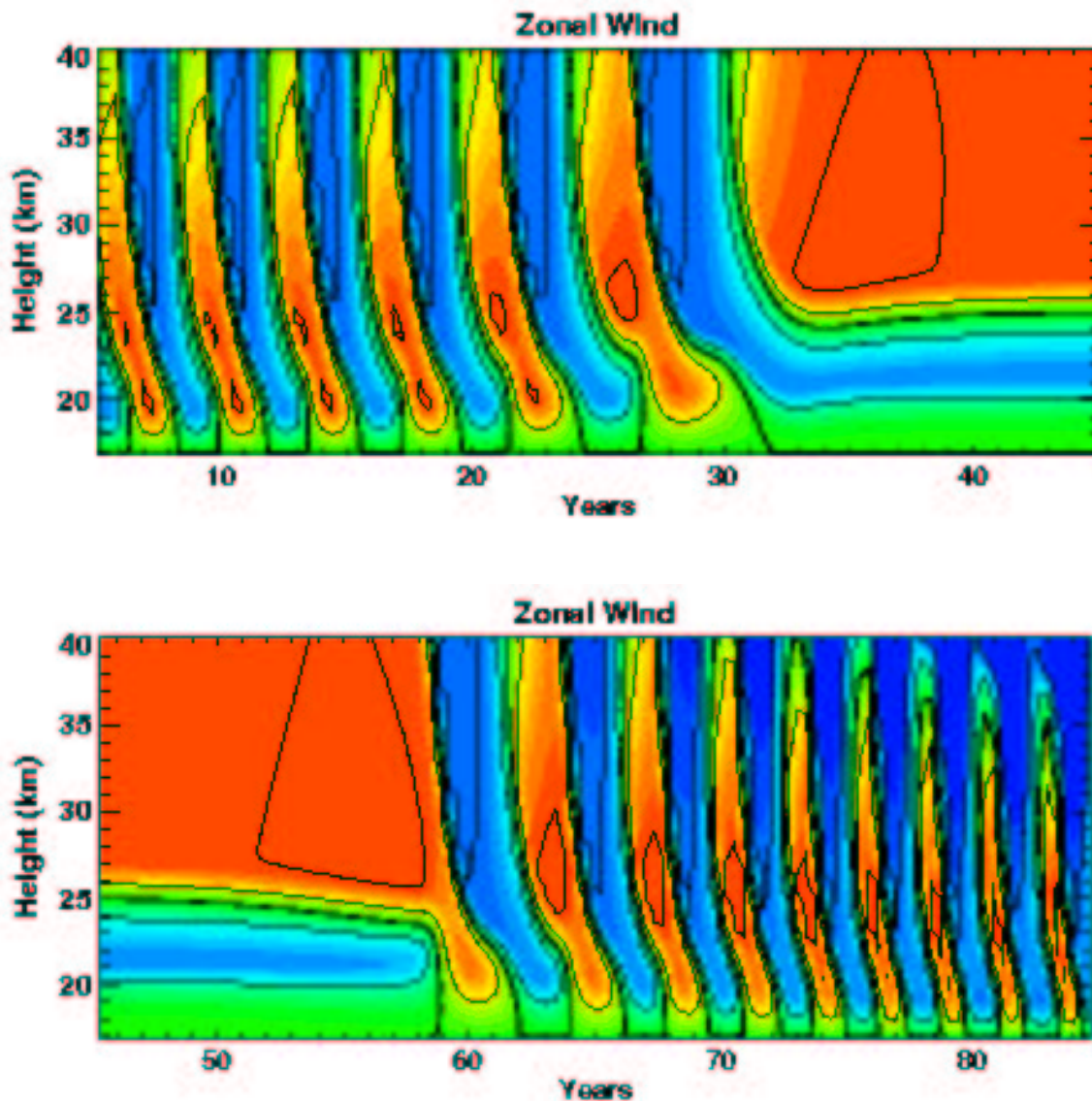
Figure 6: One-dimensional model simulation of the QBO: using equatorial planetary wave forcing and a prescribed upwelling (i.e., mean vertical wind) that increases slowly with time (top); same but with the addition of GW momentum flux using the Hines parameterization and constant upwelling (bottom). The additional flux provided by the GWs is required to offset the period-lengthening effect of the upwelling.
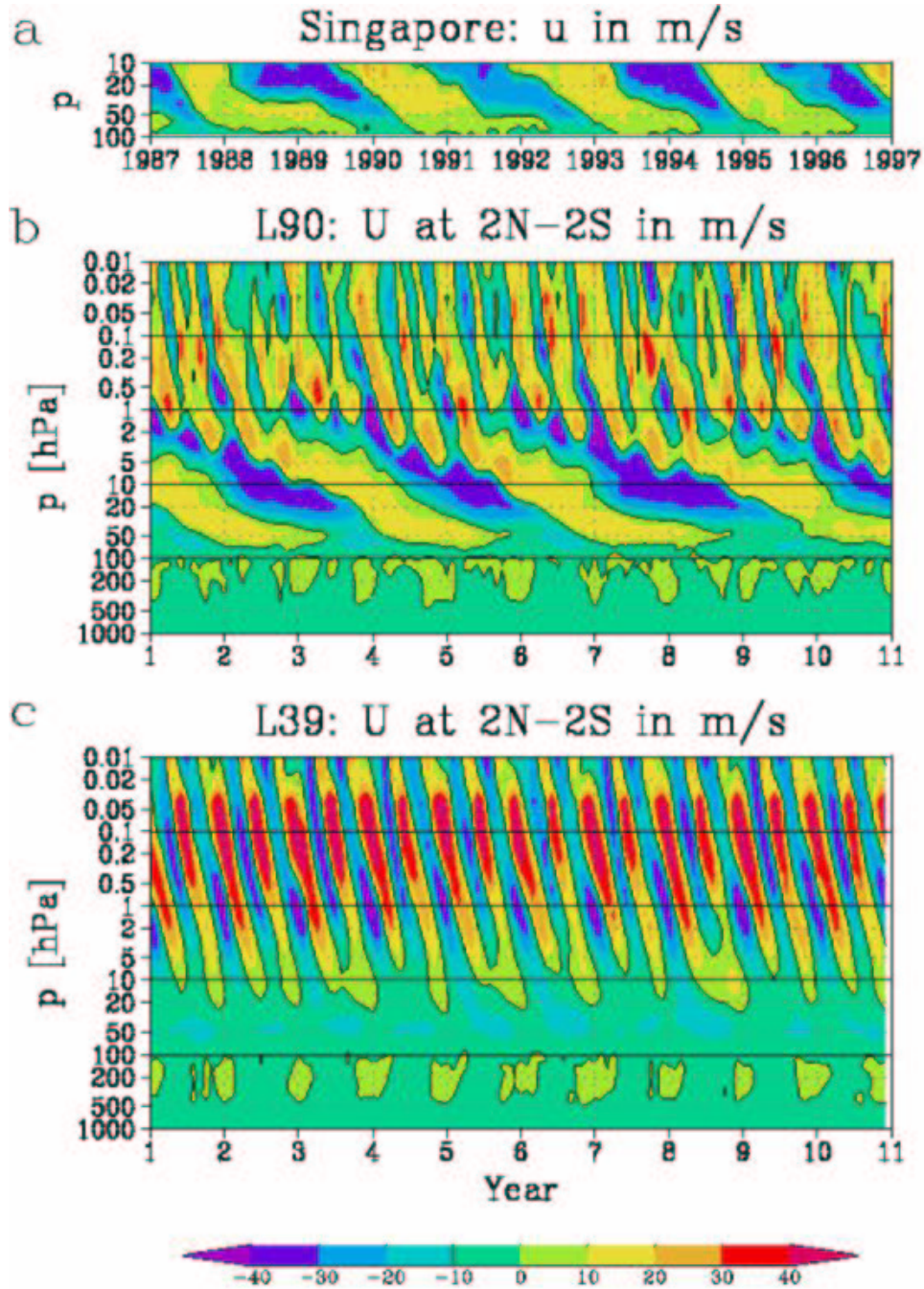
Figure 7: Observed equatorial zonal wind at Singapore (top). Simulations using the MAECHAM5 GCM with parameterized GW drag: 90 vertical levels (middle) and 39 levels (bottom). The simulated QBO in the middle panel is attributed to the better resolution of resolved waves in the stratosphere. From Giorgetta et al. (2002).
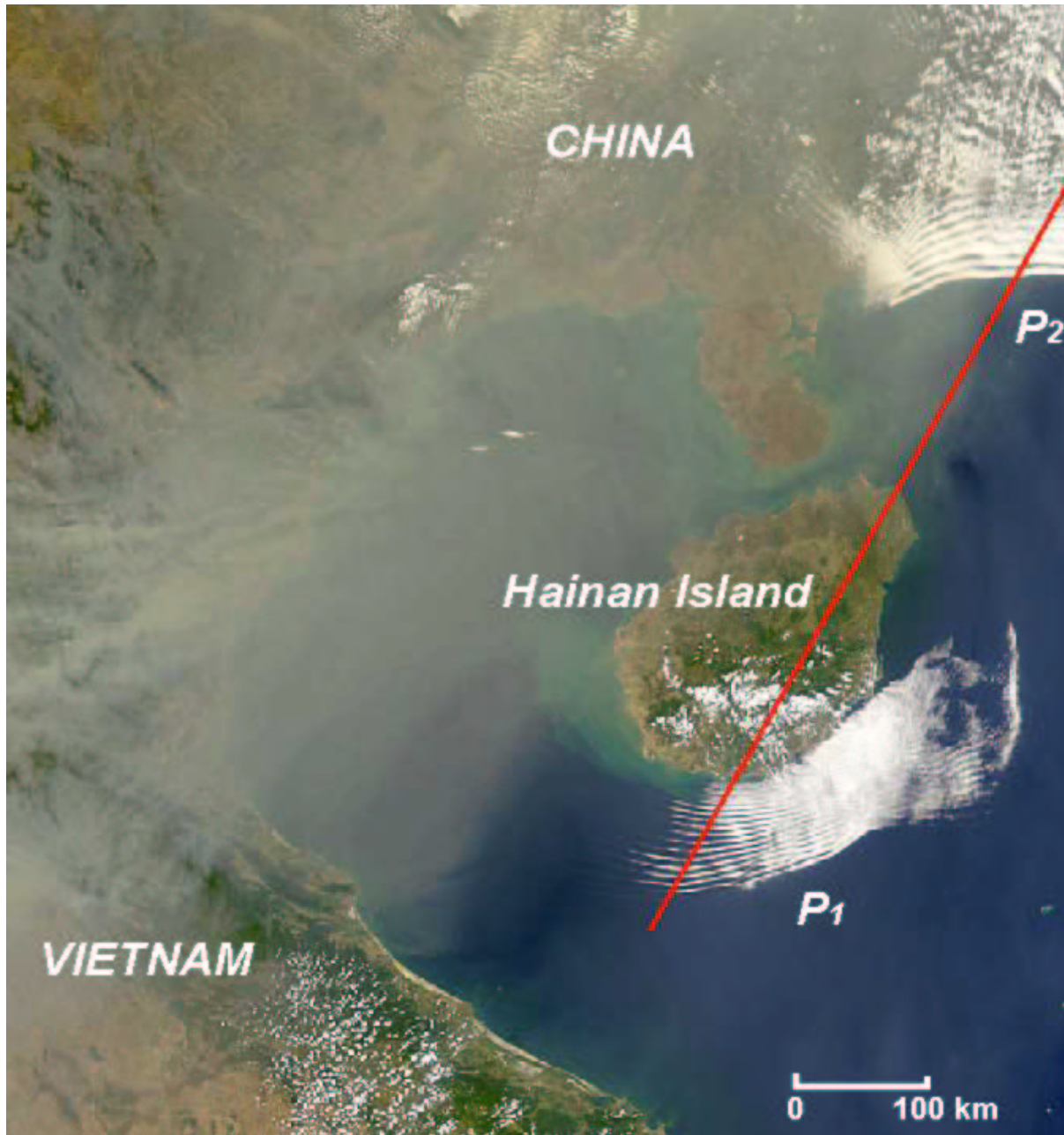
Figure 8: Satellite image of vertically trapped mountain waves (lee waves). The red line denotes the wind direction. (Image courtesy of Sam Shen, University of Alberta).
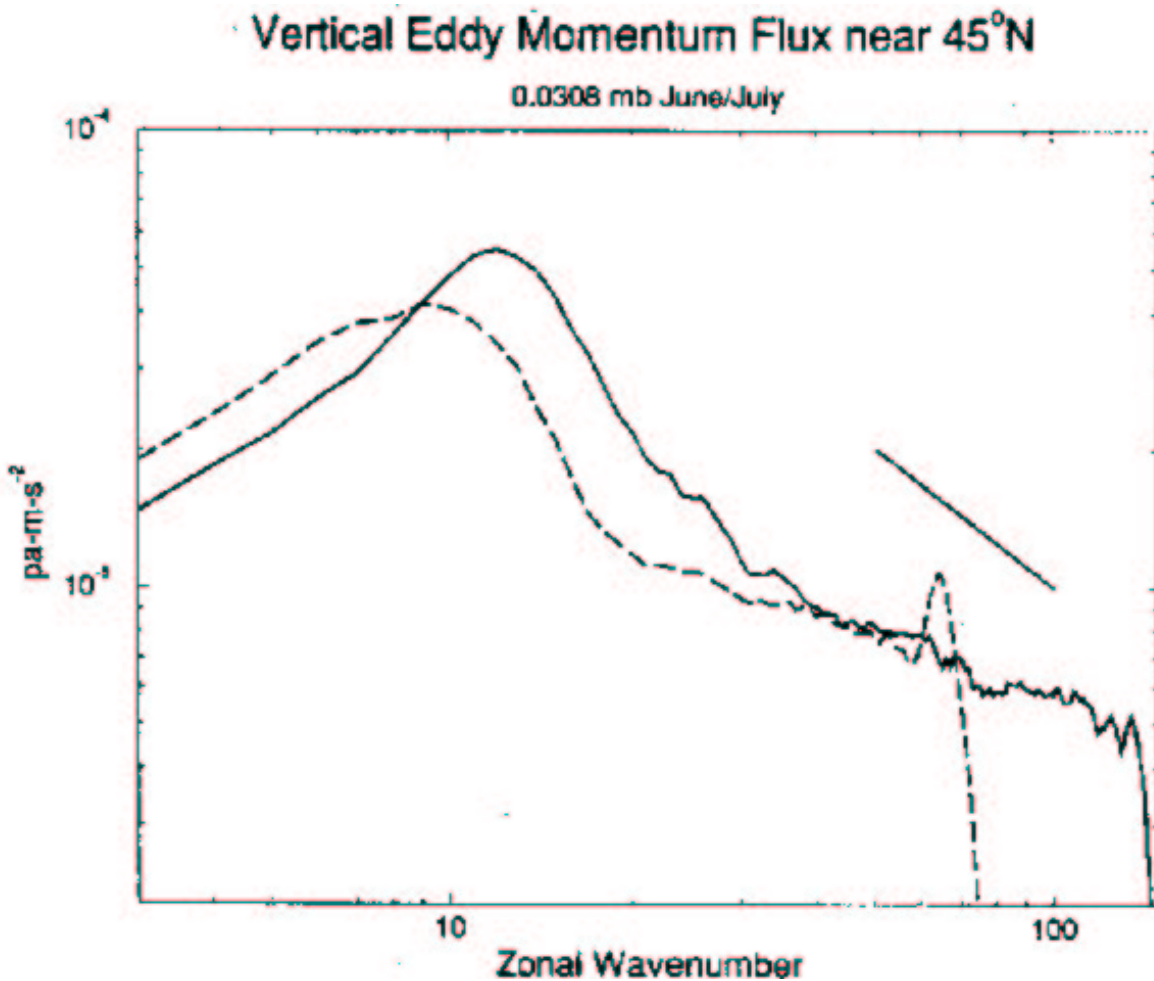
Figure 9: Vertical flux of horizontal momentum as a function of zonal wavenumber at ~ 70 km from the SKYHI GCM using a $1° \times 1.2°$ resolution (solid) and $2° \times 2.4°$ resolution (dashed). The shallow slope at high wavenumber means that much higher horizontal resolution is required to capture most of the wave momentum flux. From Hamilton (1996).

With orographic GWD (JJA)

With orographic GWD (DJF)

Without orographic GWD (JJA)
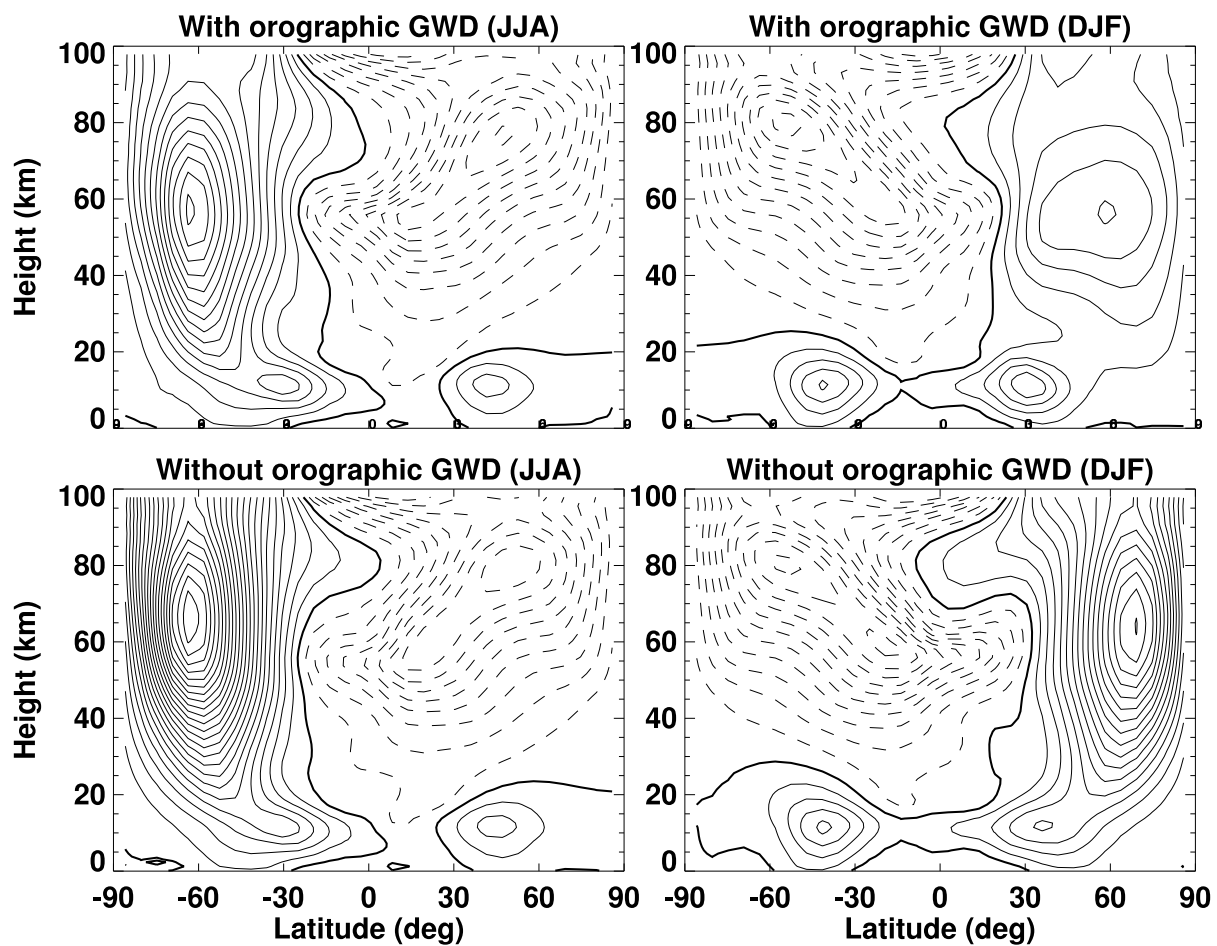
Without orographic GWD (DJF)

Figure 10: Zonal mean zonal wind from the CMAM for the seasons JJA and DJF: with orographic GWD (top) and without (bottom). Contour interval is 10 m/s. Easterlies are dashed.
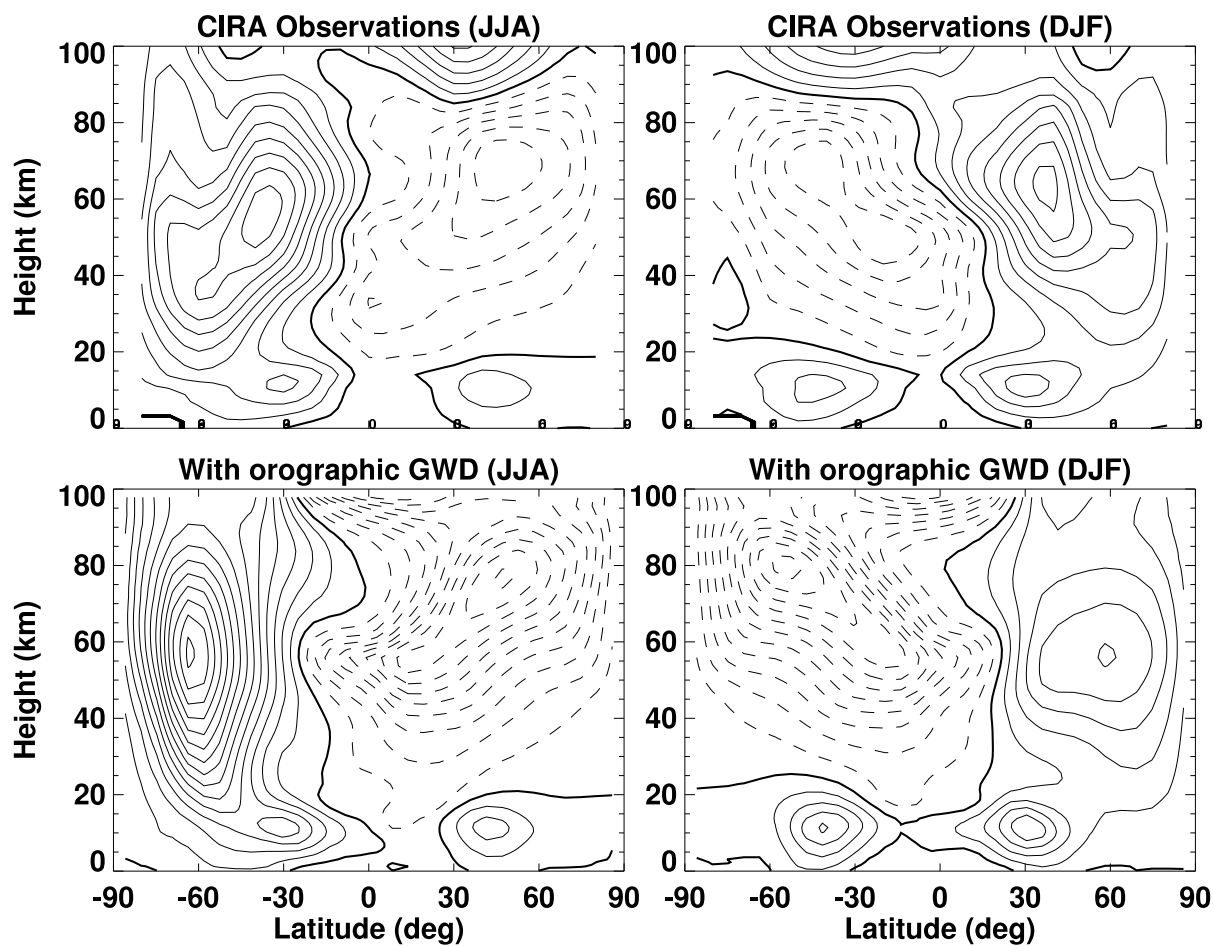
Figure 11: Zonal mean zonal wind for JJA and DJF: CIRA observations (top) and the CMAM simulation with orographic GWD (bottom). Contour interval is 10 m/s. Easterlies are dashed.
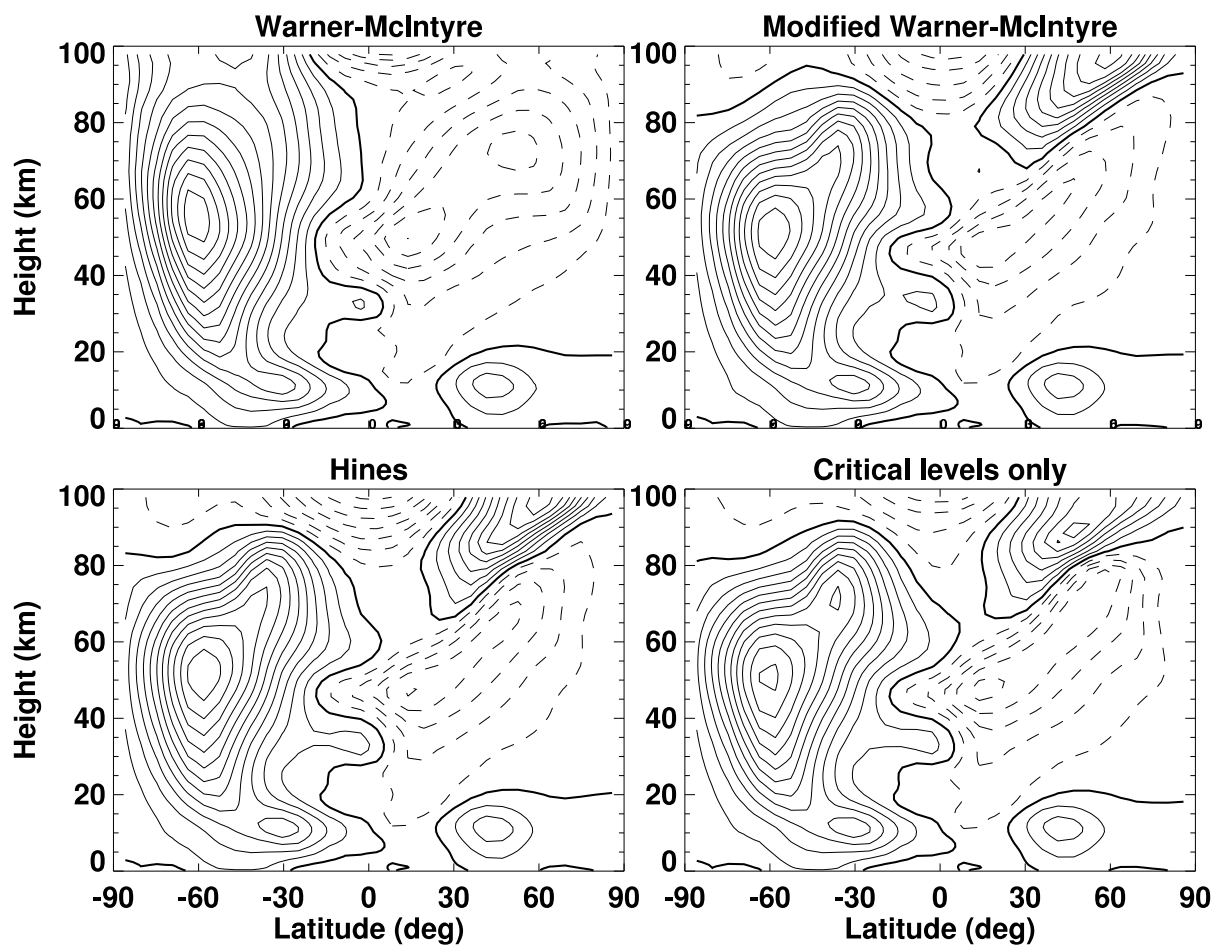
Figure 12: Zonal mean zonal wind from the CMAM for JJA: using Warner-McIntyre GWD (top left), modified Warner-McIntyre GWD (top right), Hines GWD (bottom left), and with only critical levels, i.e., no saturation, (bottom right). Contour interval is 10 m/s. Easterlies are dashed.
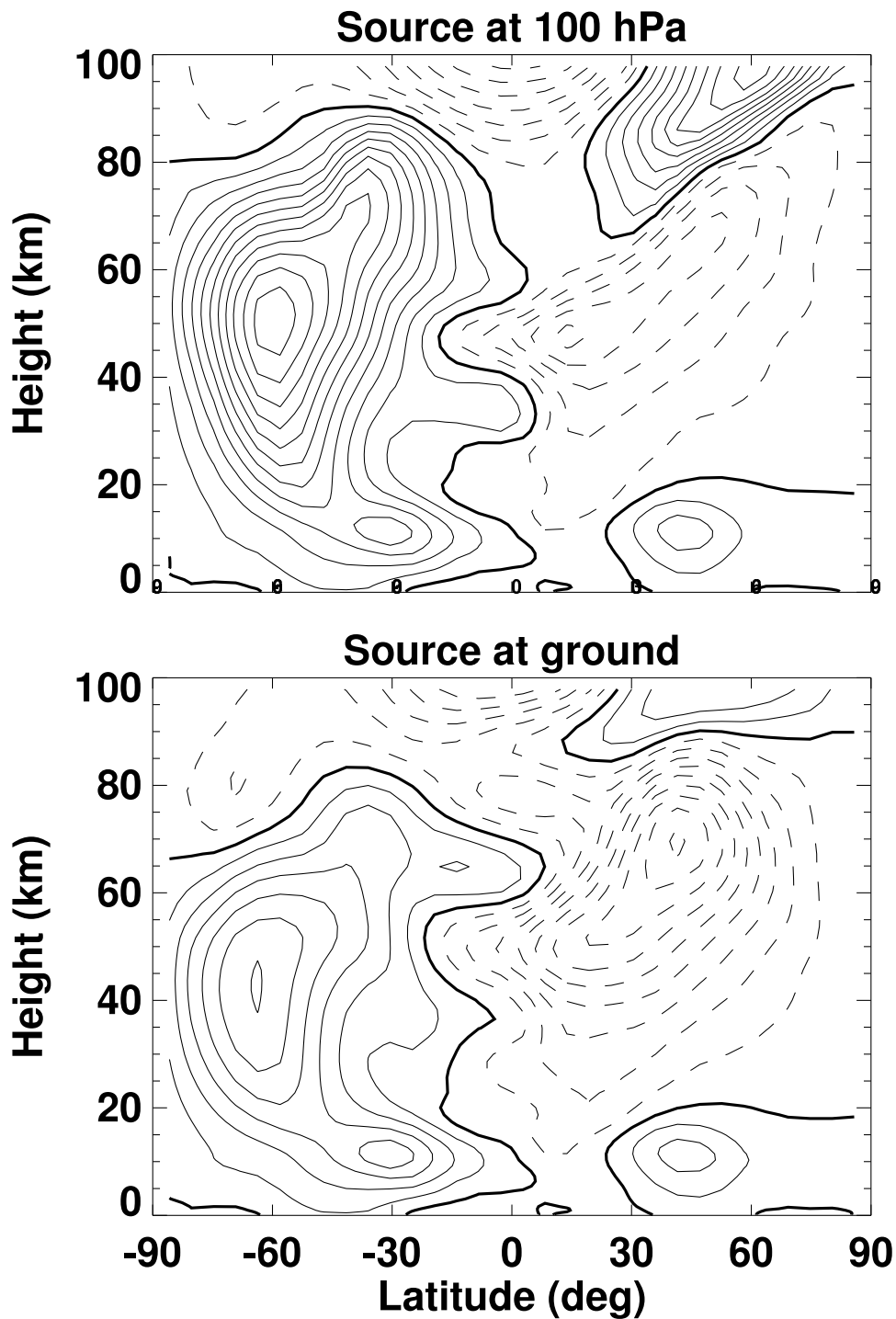
Figure 13: Zonal mean zonal wind from the CMAM for JJA: GW source at 100 hPa (top) and at the ground (bottom). Hines GWD is used. Contour interval is 10 m/s. Easterlies are dashed.
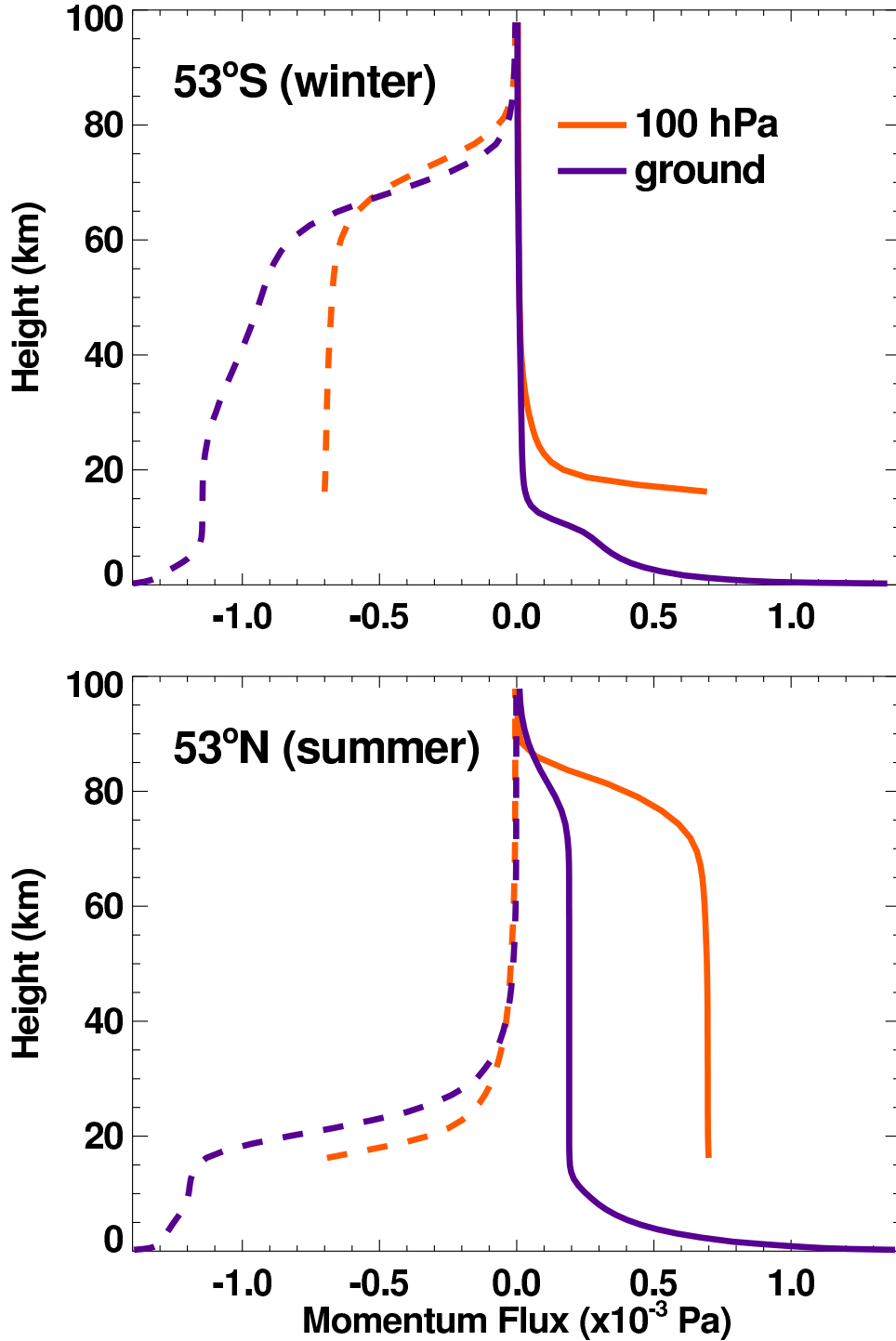
Figure 14: Eastward and westward components of the zonal mean GW momentum flux from the CMAM for JJA: 53°S (top) and 53°N (bottom). Using Hines GWD with GW source at 100 hPa and the ground.

Meridional Wind (m/s) at 12Z for April

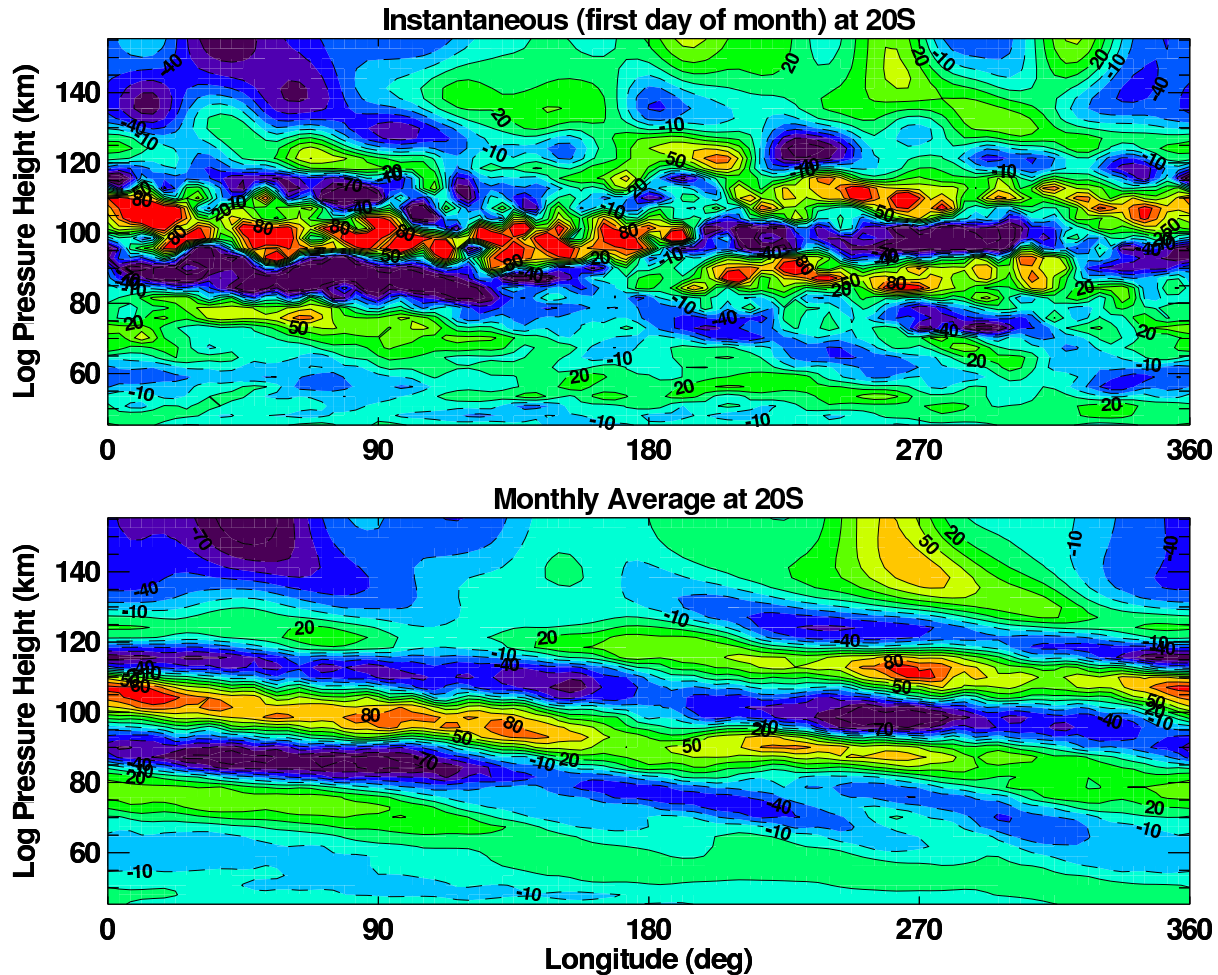**CMAM (experiment = UAM1A; year = 3)**

Figure 15: Meridional wind component at 12 hours local solar time at the latitude 20°S from the extended version of the CMAM: instantaneous value (top) and monthly mean (bottom). The banded structure seen in the monthly mean is the migrating diurnal tide (i.e., a planetary-scale gravity wave). The short horizontal scale disturbances seen in the snapshot are (resolved) gravity waves; note how they increase in amplitude up to ~ 110 km, after which they are rapidly dissipated by molecular diffusion.
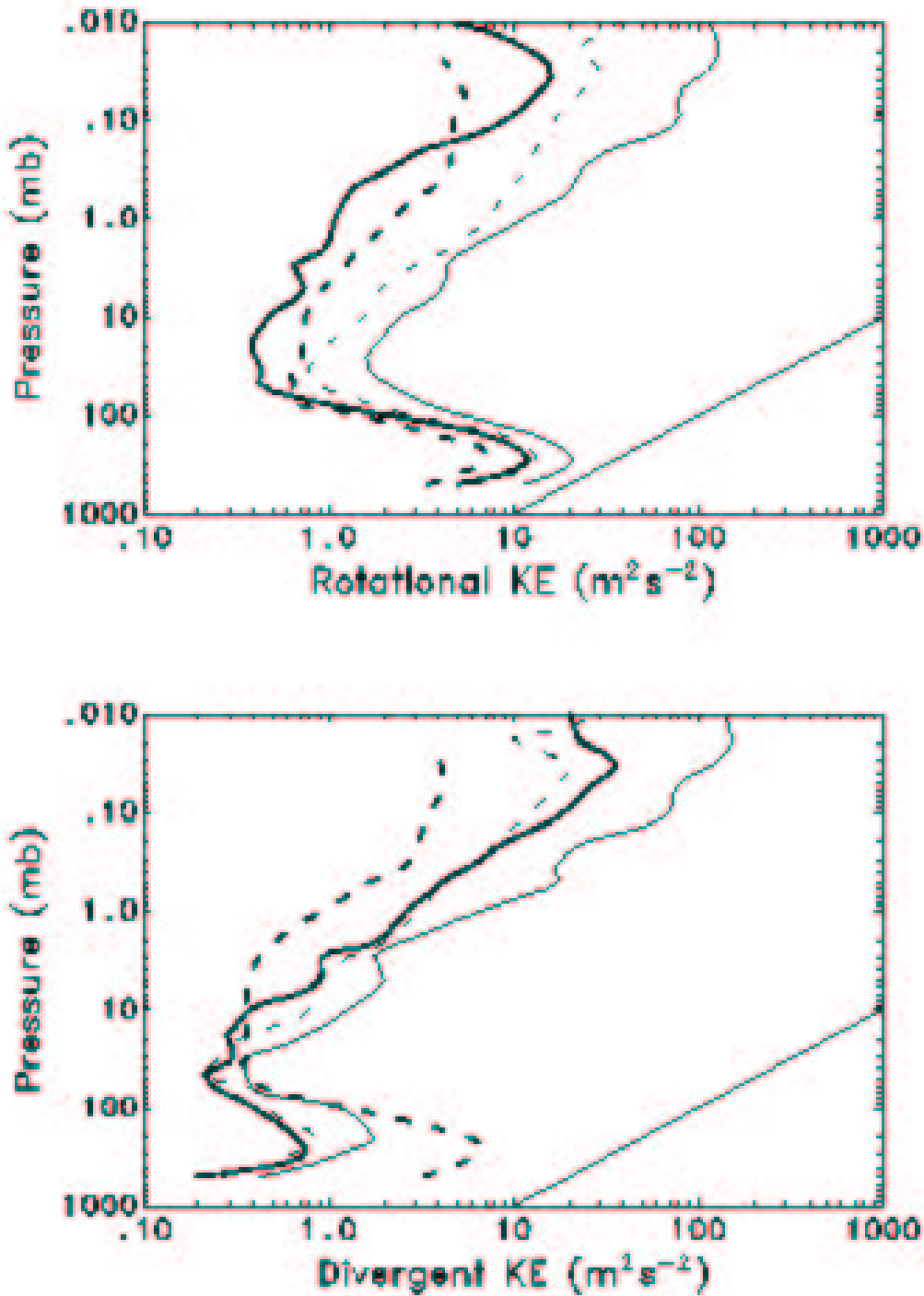
Figure 16: Rotational (top) and divergent (bottom) components of the kinetic energy per unit mass for 4 different GCMs. The profiles are obtained by averaging the spectra over the total horizontal waveumber from $15 \leq n \leq 30$. The CMAM is the thin solid line. From Koshyk et al. (1999).
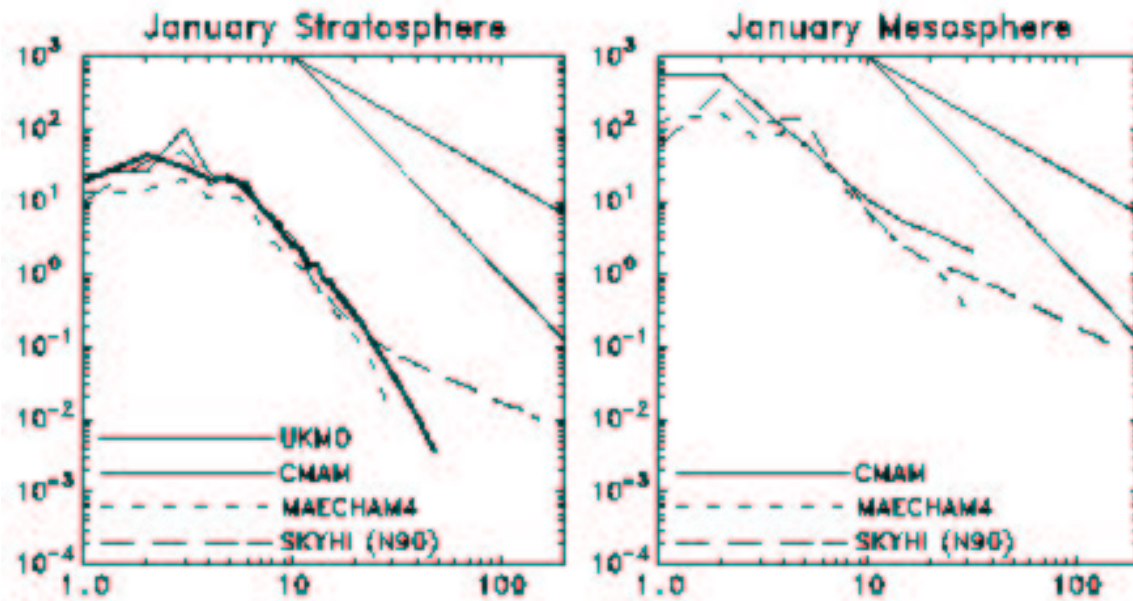
Figure 17: Kinetic energy per unit mass (vertical axis) vs total horizontal wavenumber (horizontal axis) in the stratosphere and mesosphere for different GCMs. Note how the mesospheric spectra are much shallower than the stratospheric spectra. This is an indication of (resolved) vertically propagating gravity waves. From Koshyk et al. (1999).
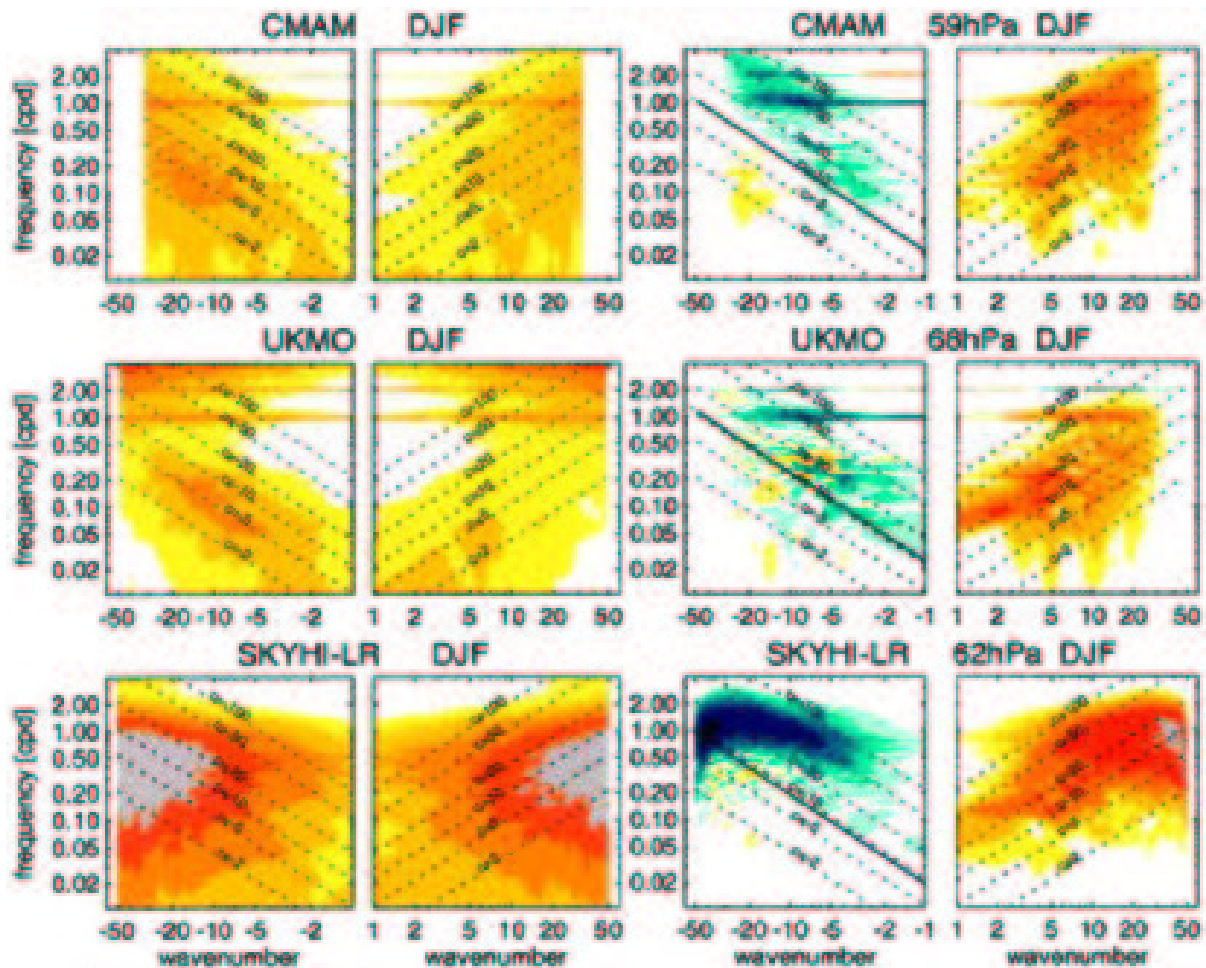
Figure 18: Zonal wavenumber-frequency spectra of precipitation rate (left panels) and vertical component of the Eliassen-Palm flux at 70 hPa for 3 different GCMs. The spectra have been averaged between 10°S to 10°N for DJF. The differences in the (resolved) EP flux are attributed to differences in the convective heating parameterizations (which generates the precipitation) used in the models. From Horinouchi et al. (2003).
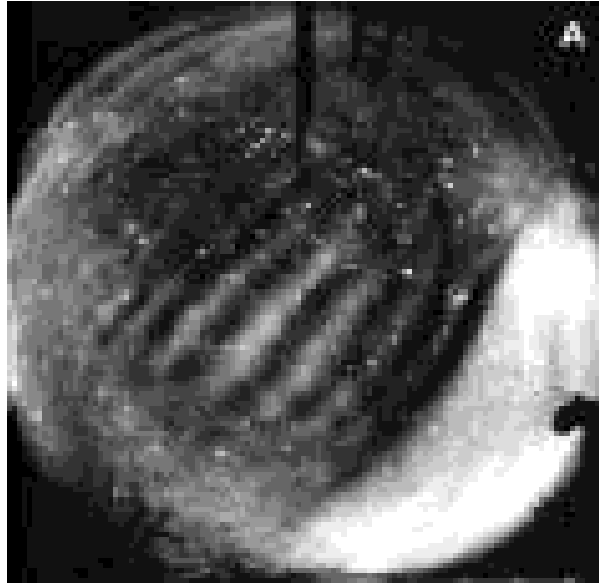
Figure 19: Gravity waves in the "green-line" airglow layer (~ 95 km) photographed using an all-sky imager during the Aloha'93 campaign in Hawaii (top) (Photo credit Mike Taylor). Gravity waves in mesospheric noctilucent clouds (bottom) (Photo credit unknown).
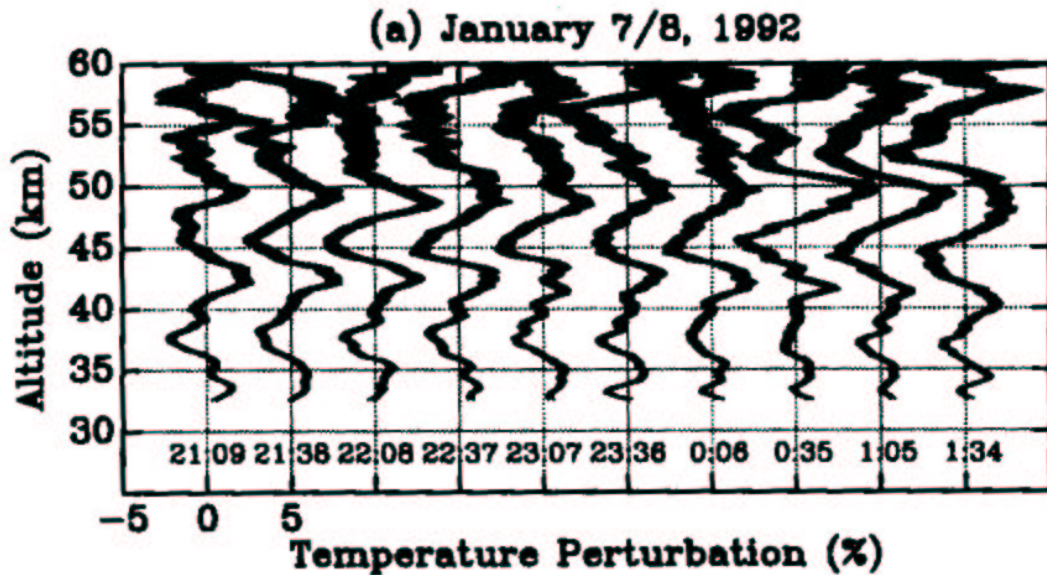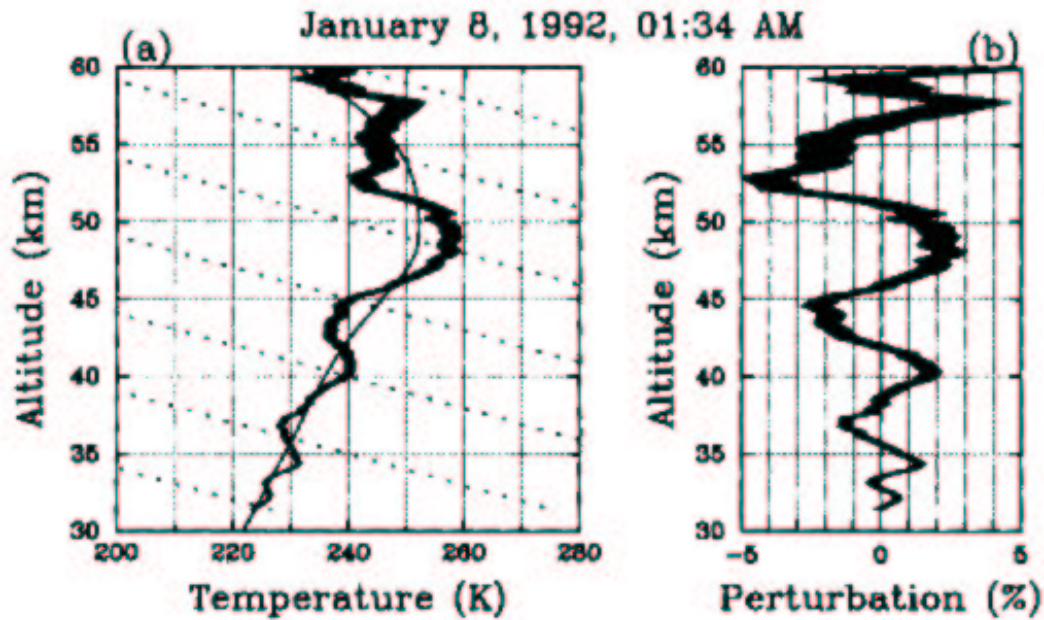
Figure 20: Temperature measured by a Rayleigh lidar at York University, Toronto, (top left) and the corresponding fractional perturbation, which is derived by removing the background profile, (top right). The perturbation is interpreted as a vertically propagating gravity wave with a vertical wavelength of ~ 8 km and an amplitude which increases with height. Sequence of fractional temperature perturbations at 30 minute intervals (bottom). The downward propagation of the phase indicated upward energy propagation of the GW. From Whiteway and Carswell (1995).
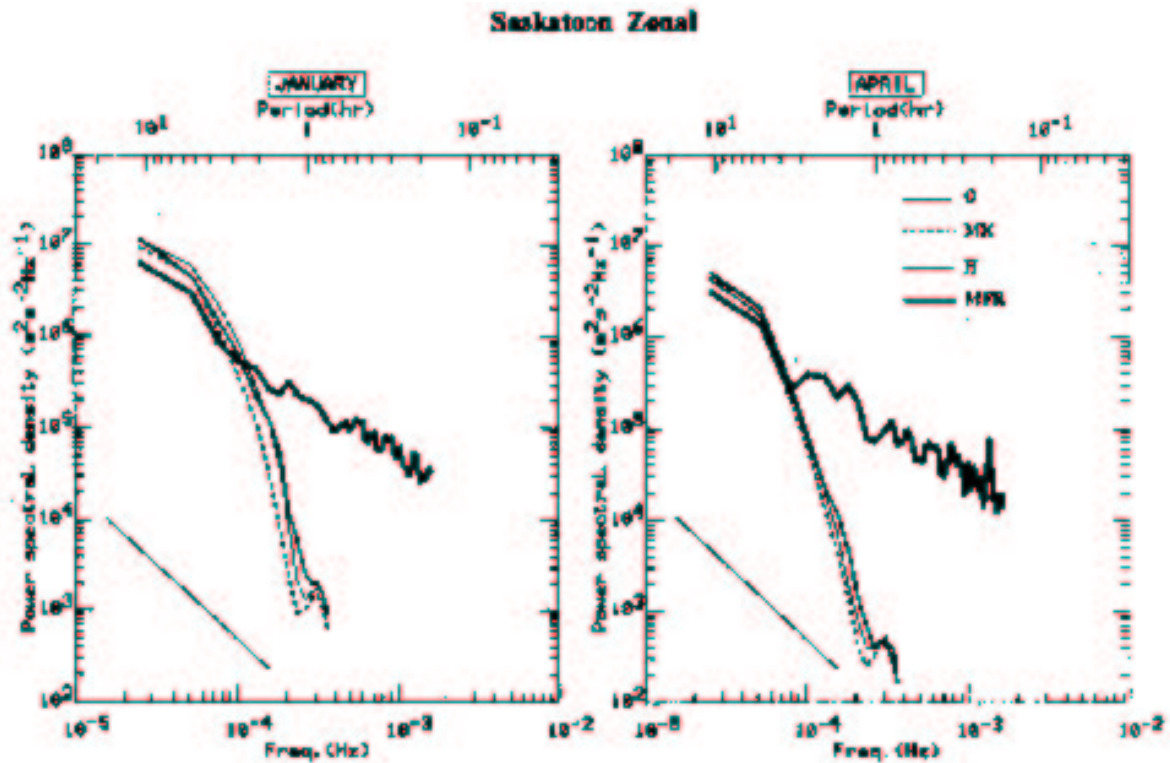
Figure 21: Horizontal wind power spectra versus frequency at ~ 75 km at Saskatoon, Saskatchewan: MF radar results are denoted by the thick solid line. Results from three different simulations of the CMAM are given by the thin lines. For periods less than ~ 3 hours the power in the CMAM spectra drop off much more rapidly than the observations. This behaviour results from the temporal smoothing of high frequency gravity-wave oscillations in the CMAM. From Manson et al. (2002).
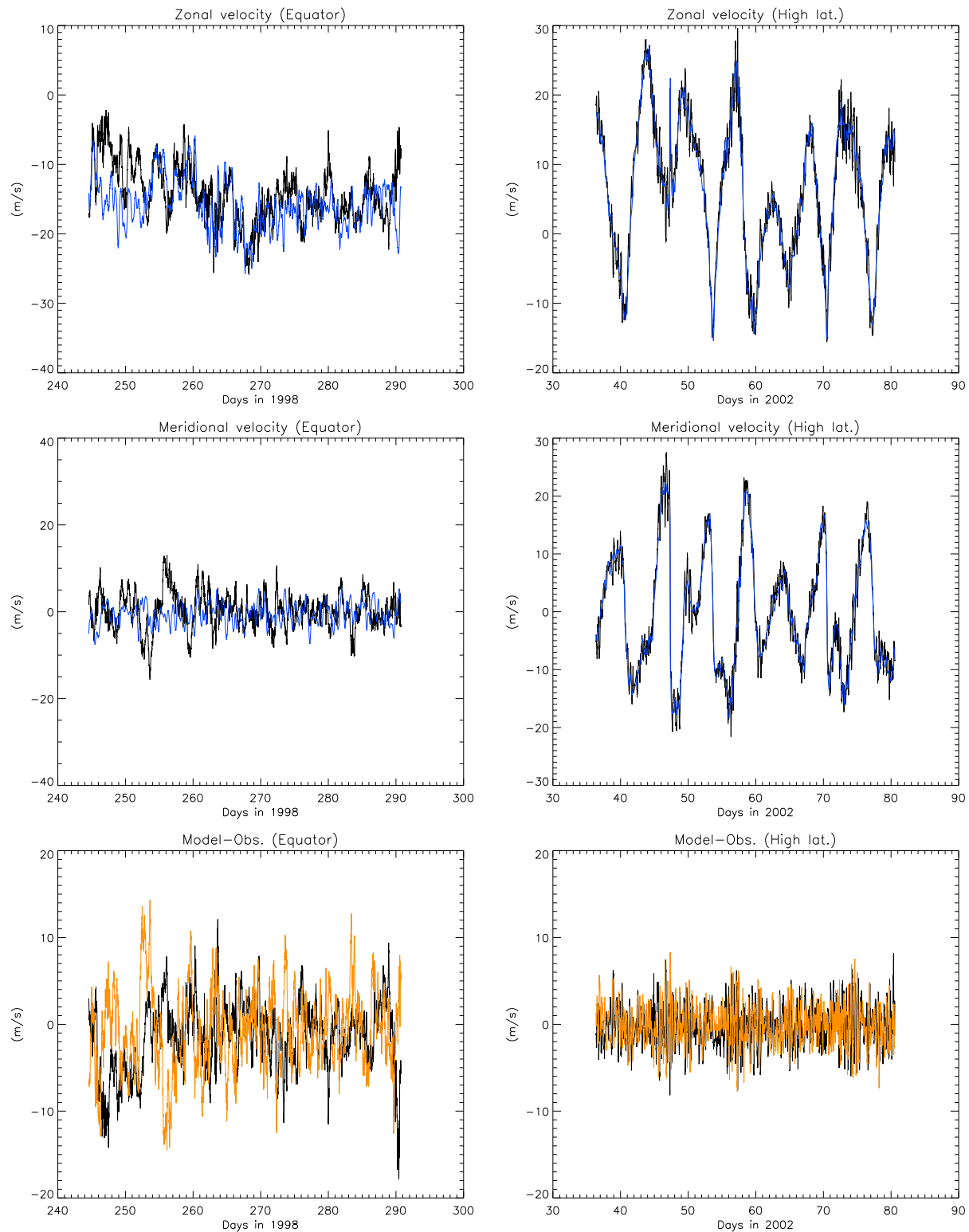
Figure 22: Horizontal winds measured during super-pressure balloon flights at ∼ 20 km in the tropics (left) and high latitudes (right) in black. The high frequency oscillations seen in the 2 top right panels are inertia gravity waves. The blue curves are analyzed winds. Figure courtesy of Albert Hertzog.
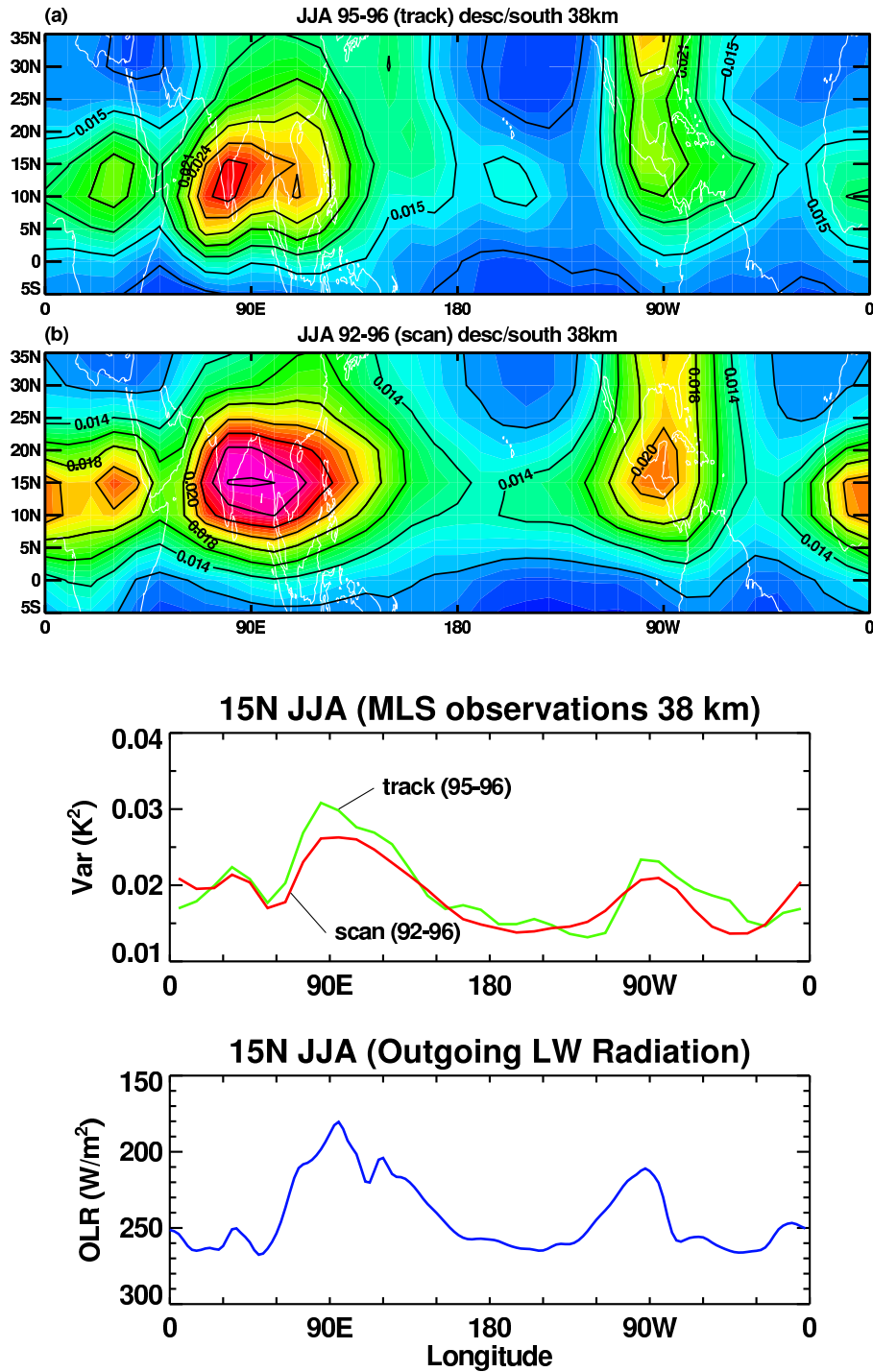
Figure 23: Temperature variances derived from Microwave Limb Sounder (MLS) radiances for June, July and August at 38 km. Top two panels: variances from limb-tracking and limb-scanning modes as a function of latitude and longitude. Bottom two panels: the strong correspondence between the variances and outgoing LW radiation (low OLR means high clouds) is strongly suggestive of convective forcing of GWs. From McLandress et al. (2000).